# Characteristics of free and submerged hydraulic jumps over different macroroughnesses

Amir Ghaderi, Mehdi Dasineh, Francesco Aristodemo
and Ali Ghahramanzadeh

## ABSTRACT

The present study deals with numerical simulations of the free and submerged hydraulic jumps over different shapes of roughness in various roughness arrangements and different Froude number conditions. The models were studied using three roughness shapes, i.e. triangular, square and semi-oval for $0.2 < T/I < 0.5$, where $T$ and $I$ are height and distance of roughness, respectively. The results showed that the numerical model is fairly well able to simulate the free and submerged jump characteristics. The effect of roughness plays a role in the reduction of the relative maximum velocity which is greater in the submerged jump. The thickness of the boundary layer for both free and submerged jumps decreases with increasing the distance between the roughnesses. Triangular macroroughness has a significant effect on the length of the jump and shortest length with respect to the other shapes. The reduction in the submerged depth ratio and tailwater depth ratio depends mainly on the space of the roughnesses. The highest shear stress and energy loss in both jumps occur in a triangular macroroughness (TR) with $T/I = 0.50$ compared to other ratios and modes. The numerical results were compared with previous studies and relationships with good correlation coefficients were presented for the mentioned parameters.

**Key words** | energy loss, FLOW-3D model, flow field, hydraulic jumps, macroroughnesses

**Amir Ghaderi** (corresponding author)
Department of Civil Engineering, Faculty of Engineering,
University of Zanjan,
Zanjan,
Iran
and
Department of Civil Engineering,
University of Calabria,
via P. Bucci, Cubo 42B,
87036 Arcavacata di Rende, Cosenza,
Italy
E-mail: *amir_ghaderi@znu.ac.ir*

**Mehdi Dasineh**
Department of Civil Engineering, Faculty of Engineering,
University of Maragheh,
Maragheh, East Azerbaijan,
Iran

**Francesco Aristodemo**
Department of Civil Engineering,
University of Calabria,
via P. Bucci, Cubo 42B, 87036 Arcavacata di Rende,
Cosenza,
Italy

**Ali Ghahramanzadeh**
Department of Civil Engineering, Faculty of Engineering,
Urmia University,
Urmia, West Azarbaijan,
Iran

## HIGHLIGHTS

- CFD model is fairly well able to simulate the free and submerged jump characteristics.
- Roughness plays a role in the reduction of the relative maximum velocity, the submerged depth ratio.
- The thickness of the boundary layer for both free and submerged jumps decreases with increasing the distance between the roughnesses.
- Shear stress and energy loss in the free and submerged jumps increase in the roughnesses.

## NOTATIONS

The following symbols and their meanings are used in this paper:

| | | |
|---|---|---|
| $Q$ | l/s | Discharge |
| $D$ | m | Gate opening |
| $E_1, E_2$ | m | Specific energy at the beginning and after the free jump |
| $E_3, E_4$ | m | Specific energy at the beginning and after the submerged jump |
| $\Delta E$ | m | Energy loss |
| $y_1$ | m | Inlet depth of the hydraulic jump |
| $y_2$ | m | Sequent depth of the free jump |
| $y_3$ | m | Submerged depth |
| $y_4$ | m | Tailwater depth |
| $y_2*$ | m | Subcritical depth of the classical hydraulic jump |
| $L_{jf}$ | m | Length of the free jump |
| $L_{js}$ | m | Length of the submerged jump |
| $P_1, P_2$ | pa | Pressure before and after the jump |
| $M_1, M_2$ | kgm/s | Momentum before and after the jump |
| $F_\tau$ | N | Shear force per unit width |
| $U_{max}$ | m/s | Maximum horizontal velocity |
| $u_1$ | m/s | Inlet horizontal velocity |
| $g$ | m/s$^2$ | Gravitational acceleration |
| $I$ | m | Distance of triangular roughness |
| $T$ | m | Roughness height |
| $Fr_1$ | – | Inlet Froude number |
| $Re_1$ | – | Inlet Reynolds number |
| $S$ | – | Submergence factor |
| $\epsilon$ | – | Bed shear force coefficient |
| $t$ | s | Time |
| $p$ | pa | Pressure |
| $\rho$ | kg/m$^3$ | Mass density of water |
| $\mu$ | Ns/m$^2$ | Dynamic viscosity of water |
| $v$ | m$^2$/s | Kinematic viscosity of water |

## INTRODUCTION

A hydraulic jump is a rapidly varied flow that dissipates a significant amount of energy by changing the flow regime from supercritical to subcritical in a short length. The most important factor in this phenomenon is the Froude number at the beginning of the jump (Chow 1959). Free and submerged hydraulic jumps are commonly applicable to energy dissipation below hydraulic structures, such as control gates, spillways and weirs. Woodward (1917), Bradley & Peterka (1957), Rajaratnam (1968) and Hager *et al.* (1990) were among the first researchers to study free jumps. In particular, Rajaratnam (1968) stated in his results that, taking into account macroroughness, the length of the jump is significantly reduced if compared to a smooth one. Also, the submerged jump was investigated by Rao & Rajaratnam (1963) who proposed, using the principles of continuity and momentum size, relationships for the conjugate depth ratio and energy loss. Next, the hydraulic jump downstream of the spillways (Samadi-Boroujeni *et al.* 2013; AlTalib *et al.* 2019), at the location of sudden channel cross-section changes (Matin *et al.* 2008; Hassanpour *et al.* 2017) and after the gate (Mouaze *et al.* 2005; Lopardo 2013) was studied. Several studies were carried out to study the hydraulic jump on a rough bed. Ead & Rajaratnam (2002) showed that the shear stress of a rough bed is 10 times that of a smooth one. Dey & Sarkar (2008) stated that the thickness of the inner layer of the horizontal velocity distribution increases with increasing macroroughness. Abbaspour *et al.* (2009) studied the characteristic of free jump and velocity profiles on the rough bed. The energy dissipation caused by free hydraulic jump (FHJ) for different shapes of roughnesses was investigated by Tokyay *et al.* (2011), while Akib *et al.* (2015), Felder & Chanson (2018) and Roushangar & Ghasempour (2019) focused the attention on the resulting depth ratio, the relative length of the jump, the air–water flow properties and the energy dissipation on the rough bed. Habibzadeh *et al.* (2019) studied the effect of blocks downstream of the gate on the characteristics of the free and submerged jump. Pourabdollah *et al.* (2019) compared the characteristics of a free and submerged jump in a rough bed with the adverse slope. Numerical methods were used to study the characteristics of the hydraulic jump by various researchers. Federico *et al.* (2012) used the SPH model, Bayon-Barrachina & Lopez-Jimenez (2015) used the Openfoam model and Witt *et al.* (2018) used computational fluid dynamics (CFD)

methods to study free jump and Shekari *et al.* (2014) for the submerged jump. Summary of the research background of the characteristics of free and submerged jumps over the smooth and macroroughness is shown in Table 1. Although several studies have been carried out on macroroughnesses, there is still a strong need for fundamental studies on the effects of different shape elements of macroroughness and corresponding characteristics of free and submerged jumps. The present paper aimed at contributing numerically with CFD techniques to enhance the understanding of characteristics of free and submerged jumps, such as velocity field and bed shear stress, sequent and submerged depths ratio, the length of jumps and energy loss in triangular, square and semi-oval macroroughnesses through different hydraulic conditions and various geometrical arrangements.

## FREE AND SUBMERGED HYDRAULIC JUMPS

The hydraulic jump occurs in free surface flows in both free and submerged modes, where in the free type the tailwater depth ($y_4$) is equal to the sequent depth of jump ($y_2$). A submerged hydraulic jump (SHJ) occurs when the tailwater depth in an open-channel flow is larger than the sequent depth of the pre-existing free jump; in this case, the jump moves upstream and becomes submerged, air entrainment reduces and turbulence intensities are smaller than for free jump counterparts (Wu & Rajaratnam 1995). Figure 1 shows a schematic view of free and submerged jumps on a triangular rough bed, along with important hydraulic parameters of the present study. In Figure 1, $y_1$ and $y_2$ are referred to supercritical and subcritical depths of the free jump depth, respectively, and $y_3$ and $y_4$ are related to submerged and tailwater depths of the submerged jump, respectively. $L_{jf}$ and $L_{js}$ are lengths of the free and submerged jump. Also, $d$ is gate opening, and $T$ and $I$ are height and distance of macroroughnesses, respectively.

A submerged jump is characterized by the supercritical Froude number $Fr_1$ and the submergence factor $S$, defined as $(y_4 - y_2)/y_2$ (Rajaratnam 1965). Obviously, $S$ is equal to zero for the free jump and as $S$ increases above zero, we get a submerged jump of different degrees of submergence. From Figure 1, it is possible to distinguish three regions in a submerged jump: the developing, the developed and the recovering regions (Long *et al.* 1990). While the developing zone occupies as far as the potential-core zone and includes a supercritical flow region with wall jet characteristics, the developed area extends throughout the length of the roller of the horizontal axis ($L_{js}$), where a big counter-clockwise circulating free surface roller dissipates the hydraulic energy, beyond which the recovering region begins and includes a subcritical flow region.

## METHODS AND MATERIALS

### Input parameters for numerical models

In this study, the characteristics of free and submerged jump on triangular roughness (TR), square roughness (SR) and

**Table 1** | Specifications of the most studies conducted by other researchers in the present study field

| Researcher | Model types | | Bed form | | Jump types | | Froude number range | Other specification |
|---|---|---|---|---|---|---|---|---|
| | Exp. | Num. | smooth | rough | Free | Submerged | | |
| Ead & Rajaratnam (2002) | ✓ | | | ✓ | ✓ | | 4–10 | Corrugated beds |
| Dey & Sarkar (2008) | ✓ | | | ✓ | | ✓ | 2.6–4.9 | Horizontal rough beds |
| Abbaspour *et al.* (2009) | ✓ | ✓ | | ✓ | ✓ | | 3.8–8.6 | Sinusoidal corrugated bed |
| Tokyay *et al.* (2011) | ✓ | | | ✓ | ✓ | | 2.1–11 | Non-protruding rough beds |
| Shekari *et al.* (2014) | | ✓ | ✓ | | | ✓ | 3.2–8.2 | Used the volume of fluid (VOF) method |
| Witt *et al.* (2018) | | ✓ | ✓ | | ✓ | | 2.4–4.8 | Bubble clustering an air entraining |
| Habibzadeh *et al.* (2019) | ✓ | | ✓ | | ✓ | ✓ | 3.5–6.8 | Used blocks in downstream |
| Pourabdollah *et al.* (2019) | ✓ | | | ✓ | ✓ | ✓ | 4.5–9.5 | Effect of adverse slopes |
| Present study | | ✓ | | ✓ | ✓ | ✓ | 1.7–9.3 | Effect of rough shape |
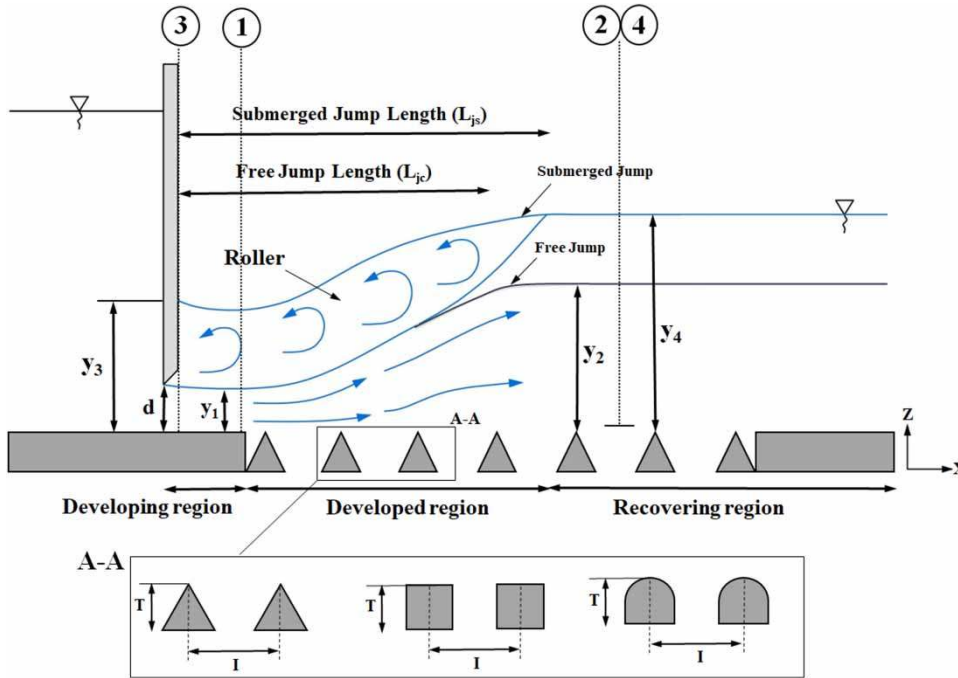
**Figure 1** │ Schematic of a free and submerged hydraulic jump on different macroroughnesses.

semi-oval roughness (OR) were investigated. Numerical simulations were performed in the range of Froude numbers ($Fr_1$) from 1.7 to 9.3 with a fixed gate opening ($d$) of 5 cm, constant roughness height of 4 cm and different $T/I$ ratios (see Figure 1).

In Table 2, standard definitions were used for the Froude and Reynolds numbers ($Fr_1 = u_1/(gy_1)^{0.5}$ and $Re_1 = (u_1 y_1)/v$, where $g$ and $v$ are gravity acceleration and water kinematic viscosity, respectively. If $y_1$ and $u_1$ are, respectively, the depth and inlet velocity of the super-critical flow just upstream of the jump, the subcritical sequent depth of the classical hydraulic jump ($y_{2*}$) is given by the well-known Belanger equation (Chow 1959; Hager 1993; Vischer & Hager 1995; Ead & Rajaratnam

2002; Tokyay 2005; Abbaspour *et al.* 2009, 2019; Chanson 2009; Samadi-Boroujeni *et al.* 2013; Hassanpour *et al.* 2017; Torkamanzad *et al.* 2019):

$$y_{2*} = \frac{y_1}{2}\left[\sqrt{(1 + 8Fr_1^2)} - 1\right] \tag{1}$$

## Computational fluid dynamics

Most applications of computational fluid dynamics (CFD) are associated with the simulation of free surface and open-channel flows, overflows, and also the simulation of the hydraulic jumps (e.g., Abbaspour *et al.* 2009; Bayon

**Table 2** │ Parameters of the numerical models

| Bed type | Q (L/s) | I (cm) | T (cm) | d (cm) | y₁ (cm) | y₄ (cm) | Fr₁ | S | Re₁ |
|---|---|---|---|---|---|---|---|---|---|
| Smooth | 30, 45 | – | – | 5 | 1.62–3.84 | 9.64–32.1 | 1.7–9.3 | 0.27–0.56 | 39,884–59,825 |
| TR | 30, 45 | 8–12–16–20 | 4 | 5 | 1.62–3.84 | 6.82–30.08 | 1.7–9.3 | 0.22–0.45 | 39,884–59,825 |
| SR | 30, 45 | 8–12–16–20 | 4 | 5 | 1.62–3.84 | 7.26–30.81 | 1.7–9.3 | 0.21–0.49 | 39,884–59,825 |
| OR | 30, 45 | 8–12–16–20 | 4 | 5 | 1.62–3.84 | 7.61–31.35 | 1.7–9.3 | 0.22–0.44 | 39,884–59,825 |

*et al.* 2016; Witt *et al.* 2018; Ghaderi *et al.* 2020a). The FLOW-3D$^{®}$ computational package was used. The software uses the Finite Volume Method (FVM) to solve the RANS equations (Reynolds Averaged Navier–Stokes) in a Cartesian, staggered grid and evaluates obstacles to the flow by the Fractional Area/Volume Obstacle Representation (FAVOR) method, presented by Hirt & Sicilian (1985). The continuity and momentum Navier–Stokes equations for 3-D incompressible flow, including FAVOR variables, are written as:

$$\frac{\partial}{\partial x_i}(\bar{u}_i A_i) = 0 \tag{2}$$

$$\frac{\partial \bar{u}_i}{\partial t} + \frac{1}{V_f}\left(\bar{u}_j A_j \frac{\partial \bar{u}_i}{\partial x_j}\right) = -\frac{1}{\rho}\frac{\partial \bar{P}}{\partial x_i} + G_i + f_i \tag{3}$$

$$f_i = \frac{1}{V_f}\left[\frac{\tau_{w,i}}{\rho} + \frac{\partial}{\partial x_j}\left(\frac{\partial \bar{u}_i}{\partial x_j} + \frac{\partial \bar{u}_j}{\partial x_i}\right)\right] \tag{4}$$

where $P$ is the pressure, $V_f$ is the volume fraction of the fluid in each cell, $A_i$ is the fractional areas open to the flow, $f_i$ is the viscous acceleration, $G_i$ is the body acceleration, $\rho$ is water density and $\tau_{w,i}$ is the wall shear stress in the subscript directions. FLOW-3D$^{®}$ uses an advanced algorithm for tracking free surface flows, called the volume of fluid (VOF) and developed by Hirt & Nichols (1981). The VOF method consists of three main components: the definition of the VOF function, a method to solve the VOF transport equation, and the setting of boundary conditions at the free surface. Within the frame of VOF methods, the interface is determined from the volume fraction $F$. The $F$ value varies between zero, when the grid cell contains no fluid, and unity when the grid cell is fully occupied with fluid, as shown in the example of Figure 2 (Ghaderi & Abbasi 2019; FLOW-3D$^{®}$ User Manual 2016). A free surface must be in cells having $F$ values between unity and zero. Since $F$ is a step function, the normal direction to the cutting line represents the free surface inside the grid cell, which is perpendicular to the direction of rapid change in $F$ values. The VOF transport equation is expressed by the following equation:

$$\frac{\partial F}{\partial t} + \frac{1}{V_F}\left[\frac{\partial}{\partial x}(F A_x u) + \frac{\partial}{\partial y}(F A_y v) + \frac{\partial}{\partial z}(F A_z w)\right] = 0 \tag{5}$$
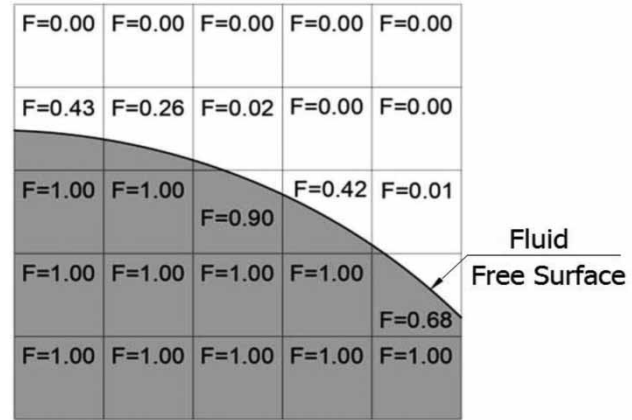


**Figure 2** │ VOF free surface assessment.

## Turbulence model

FLOW-3D$^{®}$ offers some turbulence models, such as normal turbulence models, the $k$–$\varepsilon$ turbulence model and the RNG turbulence model. In this study, the chosen turbulence model was RNG $k$–$\varepsilon$, because Flow Science Inc. (2016) mentioned that the RNG $k$–$\varepsilon$ model has wider applicability than the standard $k$–$\varepsilon$ and is usually the best choice. RNG $k$–$\varepsilon$ model can simulate the flow with a high number of computational meshes and is more accurate for rapidly strained flows and swirling flows and for lower Reynolds numbers ($Re$) based on the results of numerical studies by researchers, such as Carvalho & Lemos Ramo (2008); Daneshfaraz *et al.* (2016); Bayon *et al.* (2016); Daneshfaraz *et al.* (2019); Sangsefidi *et al.* (2019) and Ghaderi *et al.* (2020b, 2020c, 2020d, 2020e), on the acceptable ability of the RNG $k$–$\varepsilon$ turbulence model to simulate hydraulic jump in the stilling basin and flow on hydraulic structures. As a result, the RNG $k$–$\varepsilon$ was utilized to model the domain.

This model is a modified version of the $k$–$\varepsilon$ standard model, which improves its performance. The adopted scheme is a two-equation model. In particular, the first equation (Equation (6)) expresses the energy in turbulence, which is called turbulent kinetic energy (TKE) ($k$). The second equation (Equation (7)) is the turbulent dissipation rate ($\varepsilon_d$) which determines the rate of kinetic energy dissipation. These equations are expressed as follows:

$$\frac{\partial(\rho k)}{\partial t} + \frac{\partial(\rho k u_i)}{\partial x_i} = \frac{\partial}{\partial x_j}\left[\alpha_k \mu_{\text{eff}} \frac{\partial k}{\partial x_j}\right] + G_k - G_B - \rho \varepsilon_d$$
$$- Y_M + S_k \tag{6}$$

$$\frac{\partial(\rho\varepsilon_d)}{\partial t} + \frac{\partial(\rho\varepsilon_d ui)}{\partial x_i} = \frac{\partial}{\partial x_j}[\alpha_{\varepsilon d}\mu_{eff}\frac{\partial\varepsilon_d}{\partial x_j}] + C_{1\varepsilon d}\frac{\varepsilon_d}{k}(G_k$$
$$+ C_{3\varepsilon d}G_b) - C_{2\varepsilon d}\rho\frac{\varepsilon^2}{k} - R_{\varepsilon d} + S_{\varepsilon d} \qquad (7)$$

where $G_k$ is the generation of TKE caused by the average velocity gradient, $G_b$ is the generation of TKE caused by buoyancy, while $S_k$ and $S_\varepsilon$ are source terms. The values of $\alpha_k$ and $\alpha_\varepsilon$ are the inverse effective Prandtl numbers for $k$ and $\varepsilon_d$, respectively, while $\mu_{eff}$ is the effective viscosity $\mu_{eff} = \mu + \mu_t$, being $\mu_t$ the eddy viscosity.

For the above Equation (7):

$$R_\varepsilon = \frac{C_\mu\rho\eta^3(1 - \eta/\eta_0)\varepsilon^2}{k(1 + \beta\eta^3)} \qquad (8)$$

$$\mu_t = \frac{\rho C_\mu k^2}{\varepsilon} \qquad (9)$$

The constant values for this model are (Yakhot & Orszag 1986; Samma et al. 2020): $C_\mu = 0.0845$, $C_{1\varepsilon} = 1.42$, $C_{2\varepsilon} = 1.68$, $C_{3\varepsilon} = 1.0$, $\sigma_k = 0.7194$, $\sigma_\varepsilon = 0.7194$, $\eta_0 = 4.38$ and $\beta = 0.012$.

## Numerical domain

The calibration data provided by Ahmed et al. (2014) allow the comparison of the numerical model and laboratory test results. A specification of the experimental results was noticed in the validity of the numerical model part. For this experiment, a flume with the width, depth and length of, respectively, 0.75, 0.7 and 24.5 m was used (see, for more details, Ahmed et al. 2014). AutoCAD® software is used to make the geometry of the models and performed by inserting an STL (stereolithography) file. According to the experimental conditions, all boundary conditions have been employed. The inlet boundary condition was set as the discharge flow rate (Q) equal to the experimental flow exit discharge. The boundary condition at the downstream end of the domain was described by a pressure boundary condition (P) corresponding to the tailwater depth in the flume. Wall roughness has been neglected due to the small roughness of the material of the experimental facility which was used for validation. The lower Z ($Z_{min}$) and both of the side boundaries were treated as rigid wall (W).

No-slip conditions were applied at the wall boundaries and friction was neglected. No-slip is defined as zero tangential and normal velocities ($u = v = w = 0$). With a no-slip boundary, it is assumed that a law-of-the wall type profile exists in the boundary region (FLOW-3D® User Manual 2016). An atmospheric boundary condition is set to the upper boundary of the channel. This allows the flow to enter and leave the domain as null von Neumann conditions are imposed on all variables except for pressure, which is set to zero (i.e. atmospheric pressure). Symmetry boundary condition (S) is used at the inner boundaries as well. Figure 3 shows the computational domain of the present study and the associated boundary conditions.

The spatial domain subject of the present study was meshed using a structured rectangular hexahedral mesh with two different mesh blocks. Hence, a containing mesh block was created for the entire spatial domain, and then, a nested mesh block was built, with refined cells for the area of interest, where the hydraulic jump takes place (see Figure 4). This technique, i.e. a nested mesh block, was adopted from previous studies (see, for example, Choufu et al. (2019), Zahabi et al. (2018) and Ghaderi & Abbasi (2019)). Three different computational meshes were utilized to select the appropriate mesh by utilizing Grid Convergence Index (GCI), which is a widely accepted and recommended method for estimating discretization error that has been applied to several CFD cases (e.g., Bayon et al. 2016; Helal et al. 2020). The analysis was developed following the Richardson extrapolation method (Celik et al. 2008). Three different meshes with fine, medium and coarse cells, consisting of 4,624,586, 2,908,596 and 1,285,482, cells in total, respectively, were used to examine the effect of the grid size on the accuracy of the numerical results. Table 3 summarizes some details of the three computational grids.

The GCI was determined for the computed $y_3/y_1$ ratio at $Fr_1 = 4.5$ obtained from numerical solution on the three grids. Using the Richardson error estimator to compare the three grids (fine, medium and coarse grid), the fine-GCI is defined as:

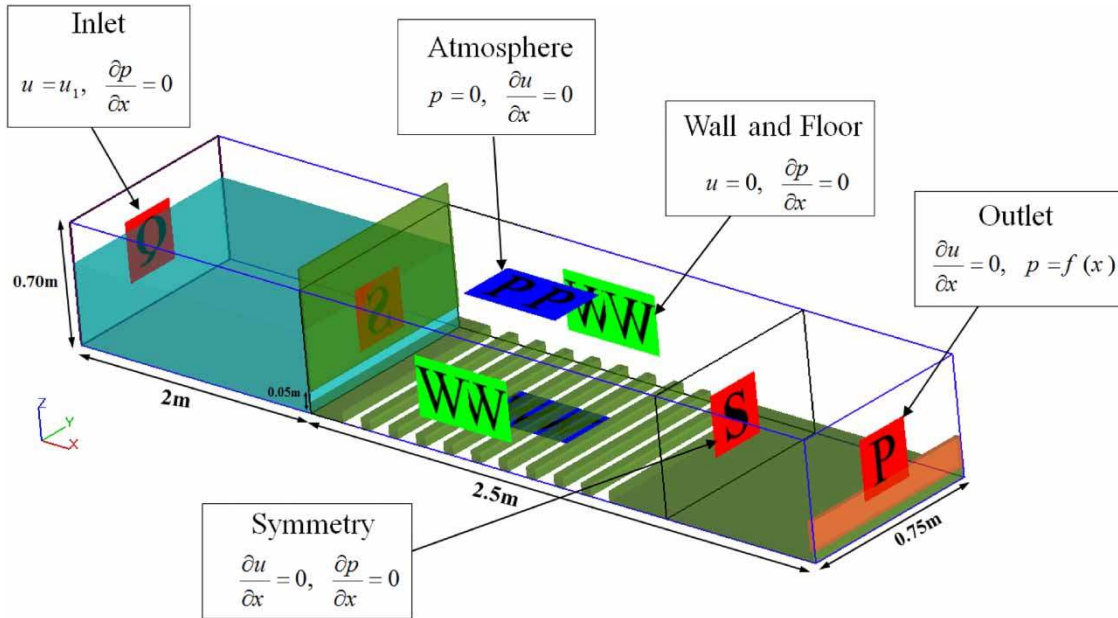$$GCI_{32}^{fine} = \frac{1.25|E_{32}|}{r_{32}^p - 1} \qquad (10)$$

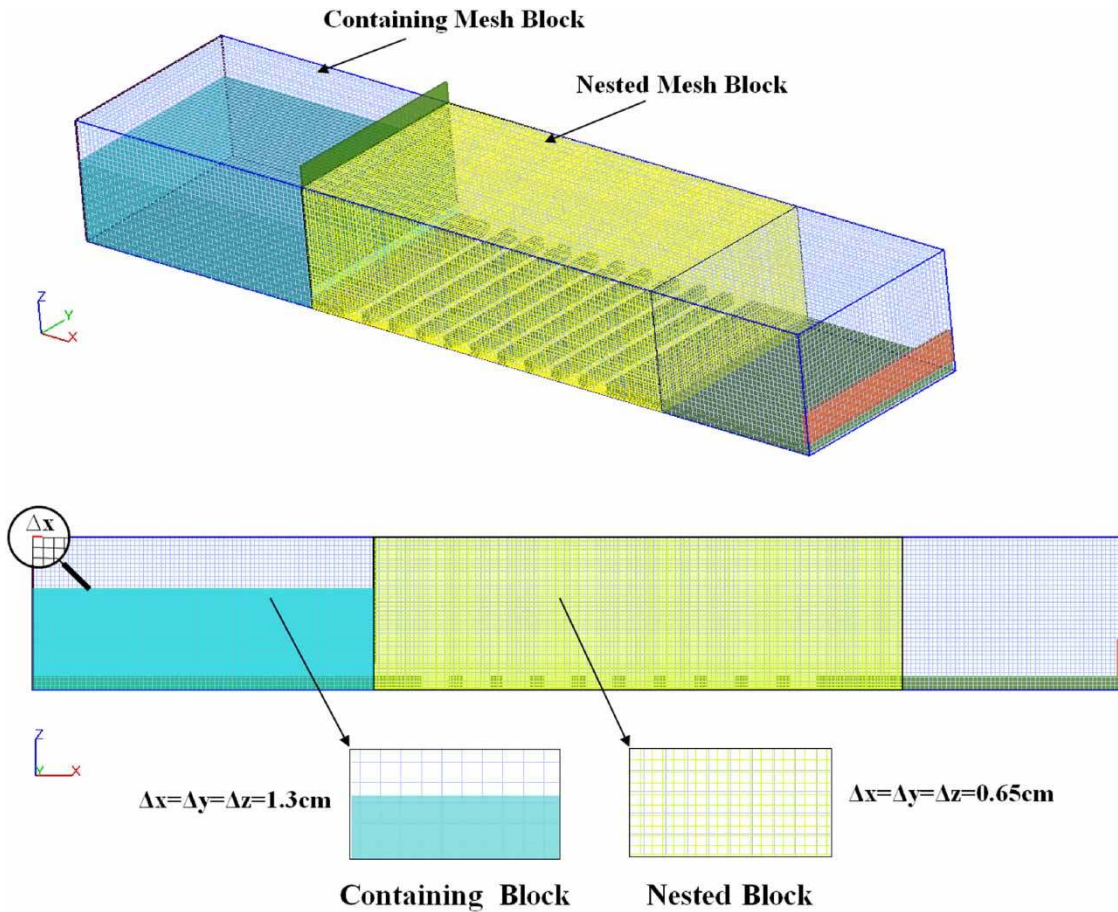**Figure 3** │ Boundary conditions on the numerical domain in FLOW-3D.



**Figure 4** │ Sketch of mesh setup.

**Table 3** │ Characteristics of the meshes tested in the convergence analysis

| Mesh | Nested block cell size (cm) | Containing block cell size (cm) |
|---|---|---|
| 1 | 0.55 | 1.10 |
| 2 | 0.65 | 1.30 |
| 3 | 0.85 | 1.70 |

where $E_{32} = (f_{s2} - f_{s3})/f_{s2}$ is the approximate relative error between the medium and fine grids, $f_{s2}$ and $f_{s3}$ are medium and fine grid solutions for $y_3/y_1$ ratios, respectively, and $p$ is the local order of accuracy. For the three-grid solutions, $p$ is obtained by solving the equation:

$$p = \frac{1}{\ln r_{32}} \ln |\varepsilon_{21} - \varepsilon_{32}| \tag{11}$$

where $\varepsilon$ is the error between two adjacent meshes, namely $\varepsilon_{21} = f_{s2} - f_{s1}$ and $\varepsilon_{32} = f_{s3} - f_{s2}$. The value of $r_{32} = G_3/G_2$ is the grid refinement factor between the medium and fine grid. $G_1$, $G_2$ and $G_3$ represent the abbreviations of grids. For the present three-grid comparisons, $G_1 < G_2 < G_3$. Table 4 shows a summary of the results of the mesh convergence analysis conducted. In this table, the values of $GCI_{21}$ and $GCI_{32}$ represent the relative change from medium to coarse and from coarse to medium mesh, respectively.

Since the GCI values for the finer grid ($GCI_{21}$) is small as compared to the coarser grid ($GCI_{32}$), it can be inferred that the grid-independent solution is nearly achieved and does not require carrying out further mesh refinements. Calculated values of $GCI_{32}/r^p GCI_{21}$ close to 1 indicate

**Table 4** │ Results of the mesh convergence analysis

| Parameters | Values |
|---|---|
| $f_{s1}$ (−) | 7.15 |
| $f_{s2}$ (−) | 6.88 |
| $f_{s3}$ (−) | 6.19 |
| $p$ (−) | 5.61 |
| $E_{32}$ (%) | 10.02 |
| $E_{21}$ (%) | 3.77 |
| $GCI_{21}$ (%) | 3.03 |
| $GCI_{32}$ (%) | 3.57 |
| $GCI_{32}/r^p GCI_{21}$ | 0.98 |

that the numerical solutions are within the asymptotic range of convergence. As a result, a mesh consisting of a containing block with a cell size of 1.3 cm and a nested block of 0.65 cm was chosen (see Figure 4).

## Near wall treatment

Usually, all the turbulence models are quite accurate and valid only to fully turbulent flows. However, near the wall, the flow is almost laminar and the turbulent stress hardly works, especially for the viscous sublayer region (Garcia Perez & Vakkilainen 2019). As a result, the traditional turbulence models do not work well here. Currently, there are two different methods (near-wall modeling method and wall function method) to solve the problem. Both methods involve a dimensionless distance $y^+$. The ratio of turbulent and laminar influences in a cell, $y^+$, is defined as:

$$y^+ = \frac{y_p u*}{v} \tag{12}$$

where $y_p$ is the distance of the first node from the wall, $u*$ is the shear velocity of the wall ($u* = \sqrt{\mu u_1/\rho y_p}$) and $v$ is the kinematic viscosity of the fluid. The near-wall modeling method directly utilizes the low Reynolds number turbulence model with many fine grids near the wall to deduce parameters in the viscous sublayer. It requires that the grid point of the first layer should be arranged within the viscous layer ($y^+ < 1$). The wall function method does not directly deduce the viscous sublayer but arranges the grid point of the first layer within the log law region ($30 < y^+ < 200 \sim 400$) and then relates the viscous layer to the log law region with empirical formulas (Salim & Cheah 2009). Compared with the near-wall modeling method, the wall function method does not need to specifically compact the grid near the wall but saves much more computation time with higher efficiency. In view of the unique grid generation technology in the FLOW-3D software, as shown in Figure 4, the grid can be flexibly adjusted to embed into the walls of the numerical model. In addition, as shown in Table 5, two different grid systems are arranged to fill the blocks to evaluate the effect of the grid size upon the numerical results. It can be noticed that the dimensionless $y^+$ in all grid systems ranges from 72 to 135.72 and confirms the

**Table 5** | Grid details in numerical domain

| Block | Max cell size (cm) | Min cell size (cm) | Near wall distance (cm) | Range of dimensionless distance $y^+$ |
|---|---|---|---|---|
| Containing and nested block | 1.3*1.3*1.3 | 0.65*0.65*0.65 | 0.5 | $72 < y^+ < 135.72$ |

requirement of the wall function method. The inlet Reynolds number varies between 39,884 and 59,825.

## Stability condition

A stability criterion similar to the Courant number is a function of time step size. The time step was calculated over each cell with the help of the CFL (Courant–Friedrichs–Lewy) criterion. During the iteration, the time step size was controlled by both of the stability and convergence criterion, which leads to time steps between 0.001 and 0.0016 s. The evolution in time was used as a relaxation to the final steady state. The steady-state convergence of the solutions was checked through monitoring the flow discharge variations at the inlet and outlet boundaries during the simulations. Figure 5 shows that $t = 16$ s is appropriate to achieve a stable steady-state condition for the adopted two discharges, i.e. $Q = 0.03$ and 0.045 m³/s. The computational time for the simulations was between 14 and 18 h using a personal computer with eight cores of a CPU (Intel Core i7-7700 K @ 4.20 GHz and 16 GB RAM).

## RESULTS AND DISCUSSIONS

### The validity of the FLOW-3D® model

A first analysis of the performance of the numerical model and laboratory test results carried out over basic variables is summarized in Table 6.

A quantitative evaluation of the computed and measured submerge ratio ($y_3/y_1$) values for submerged jump and jump depths ratio ($y_2/y_1$) values for free jump comparisons is made by using mean square error (MSE) and mean absolute relative error (MARE).

$$\text{MSE} = \frac{1}{N}\sum_{i=1}^{N}(O_i - P_i)^2 \tag{13}$$

$$\text{MARE} = \frac{1}{N}\sum_{i=1}^{N}\left|\frac{O_i - P_i}{O_i}\right| \times 100 \tag{14}$$

where $O_i$ and $P_i$ are measured and computed values,
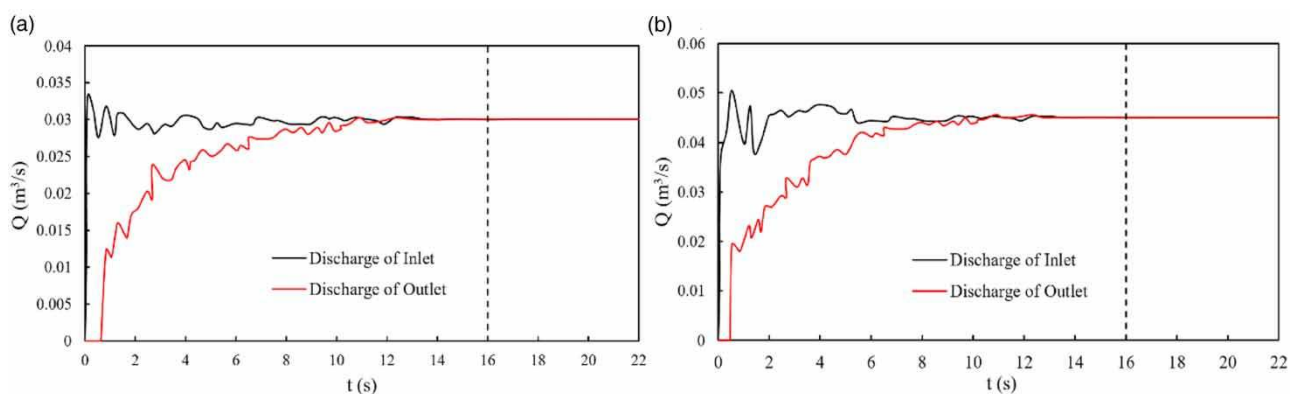


**Figure 5** | Time variation of computational fluid dynamics (CFD) flow discharge in the inlet and outlet boundaries. (a) $Q = 0.03$ m³/s, (b) $Q = 0.045$ m³/s.

**Table 6** | Basic flow variables for the numerical simulation and physical models (Ahmed *et al.* 2014)

| Models | Bed type | Q (l/s) | d (cm) | $y_1$ (cm) | $u_1$ (m/s) | $F_1$ |
|---|---|---|---|---|---|---|
| Numerical and physical models | Smooth | 45 | 0.05 | 1.62–3.83 | 1.04–3.70 | 1.7–9.3 |

respectively, and $N$ is the total number of data. Table 7 gives the results for MSE and MARE using Equations (13) and (14) for different inflow Froude numbers on the smooth bed.

Regarding the overall mean values of MSE and MARE in Table 7, it can be concluded that there is a good agreement between numerical and laboratory results. The mean maximum error is 4.21%, which confirms the ability of the numerical model to predict the specifications of the free and submerged jumps.

## Horizontal velocity distributions

The longitudinal velocity profiles on the macroroughnesses (TR, OR and SR) and smooth bed at $Fr_1 = 4.5$ after creating steady-state conditions in FLOW-3D are shown in Figure 6. It can be seen that close to the sluice gate, due to the high velocity of flow, the water depth decreases initially before it again increases to the tailwater depth $y_2$ for FHJ and $y_4$ for the SHJ. A large counter-clockwise roller exists in the upstream flow field. The zero-velocity line, where a free surface roller circulating as big counter-clockwise, dissipates the hydraulic energy and finally reaches the downstream end. From there, the velocity profile becomes more uniform. As in a fixed initial Froude number ($Fr_1$), the flow velocity decreases in the macroroughness, occurs faster than the smooth bed and the length of jump decreases. The peak of the velocity profile closer to the bed shows that the flow in this location is strongly influenced by the bed. Also, the flow velocity near the bed reduces and in the distance between the roughnesses becomes negative. This negative velocity created in the distance between the macroroughnesses (TR, OR and SR) increases with increasing the distance between the roughnesses so that for $T/I = 0.20$, it is more than the other modes as well as it is observed that the

triangular macroroughness gives the highest negative velocity with respect to the other two shapes. This is due to a clockwise recirculation zone and eddy flow exists between the roughnesses. A comparison of velocity profiles in free and submerged jumps shows that the thickness of the negative velocity layer near the flow surface is greater in submerged jumps. According to Figure 6, the horizontal velocity distribution has recovered by the time that the flow arrives at the next roughness when the distance between the macroroughnesses (TR, OR and SR) is long enough. But, if this distance is short, the flow arrives at the next roughness without adequate recovery of the horizontal velocity distribution. Hence, with an increasing number of macroroughnesses (TR, OR and SR), the rate of increase of the frictional coefficient decreases.

Figure 7 shows the dimensionless relative maximum horizontal velocity ($U_m/u_1$) versus ($X/y_1$) for the different roughness elements and for free and submerged hydraulic jumps. In Figure 7, $X$ represents the distance from the beginning of the hydraulic jump. It can be seen that the relative maximum velocity in the macroroughness is less than in the smooth one and the effect of roughness plays a role in the reduction of the relative maximum velocity which is greater in the submerged jump. The difference of the values ($U_m/u_1$) for the investigated roughness shape (TR, OR and SR) in $T/I = 0.25$ and 0.50 is not high under similar conditions and slightly lower for the TR, while the SR gives values of velocity close to the smooth bed. The boundary layer thickness ($\delta$) at each section of the hydraulic jump was equal to the depth at which the maximum velocity occurred. Therefore, the changes of the dimensionless boundary layer thickness ($\delta/y_1$) versus ($X/y_1$) are shown in Figure 8. It is observed that for both free and submerged jumps, with increasing distance from the beginning of the

**Table 7** │ MSE and MARE values for submerge ratio $y_3/y_1$ values on the smooth bed

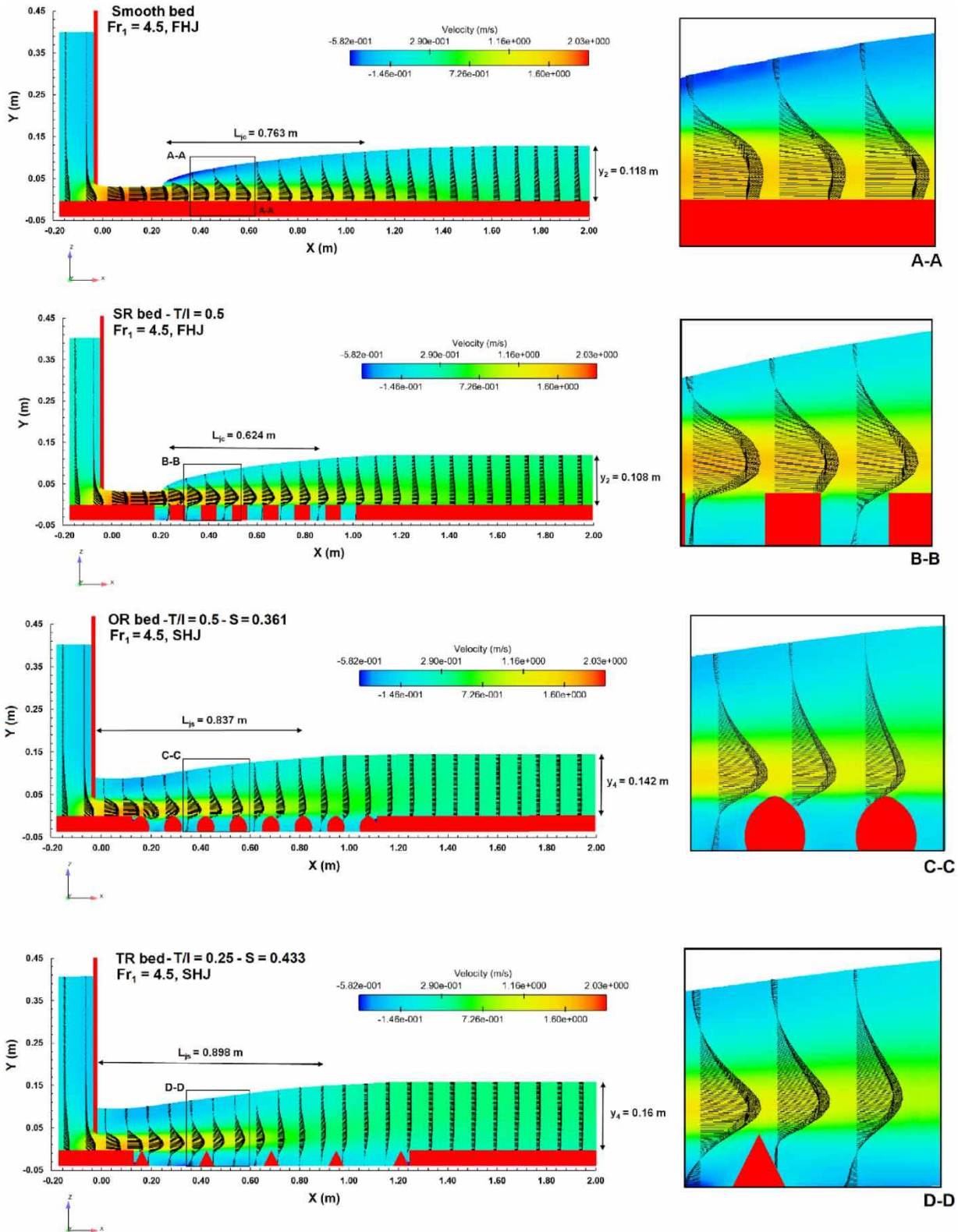| Model | $Fr_1$ | $y_3/y_1$- measured values | $y_3/y_1$- computed values | $y_2/y_1$- measured values | $y_2/y_1$- computed values | MSE (–) $y_3/y_1$ | MARE (%) $y_3/y_1$ | MSE (–) $y_2/y_1$ | MARE (%) $y_2/y_1$ |
|---|---|---|---|---|---|---|---|---|---|
| **Smooth** | 1.7 | 1.98 | 1.90 | 1.94 | 1.98 | 0.006 | 4.04 | 0.002 | 2.06 |
| **bed** | 2.5 | 3.20 | 3.16 | 2.98 | 3.09 | 0.016 | 1.25 | 0.012 | 3.70 |
| | 4.5 | 6.88 | 7.25 | 5.81 | 5.91 | 0.136 | 5.37 | 0.010 | 1.72 |
| | 6.1 | 10.02 | 9.19 | 8.08 | 8.17 | 0.689 | 8.28 | 0.010 | 1.11 |
| | 9.3 | 15.67 | 15.34 | 12.58 | 12.69 | 0.109 | 2.10 | 0.012 | 0.87 |
| | **Mean** | | | | | 0.188 | 4.21 | 0.010 | 1.89 |

**Figure 6** │ Typical longitudinal velocity profiles for the different models at $Fr_1 = 4.5$.
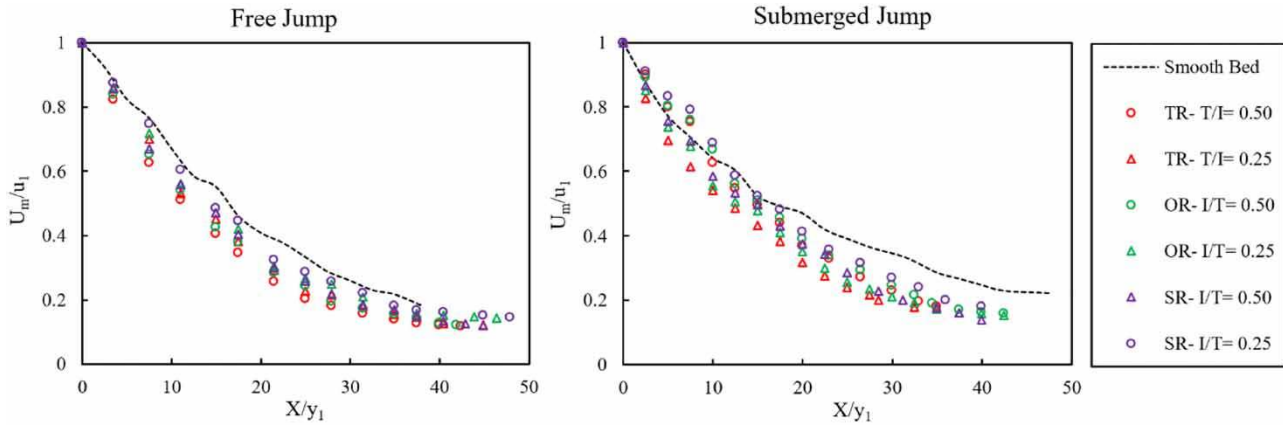
**Figure 7** | Variations of ($U_m/u_1$) vs. ($X/y_1$) for different roughness shape.
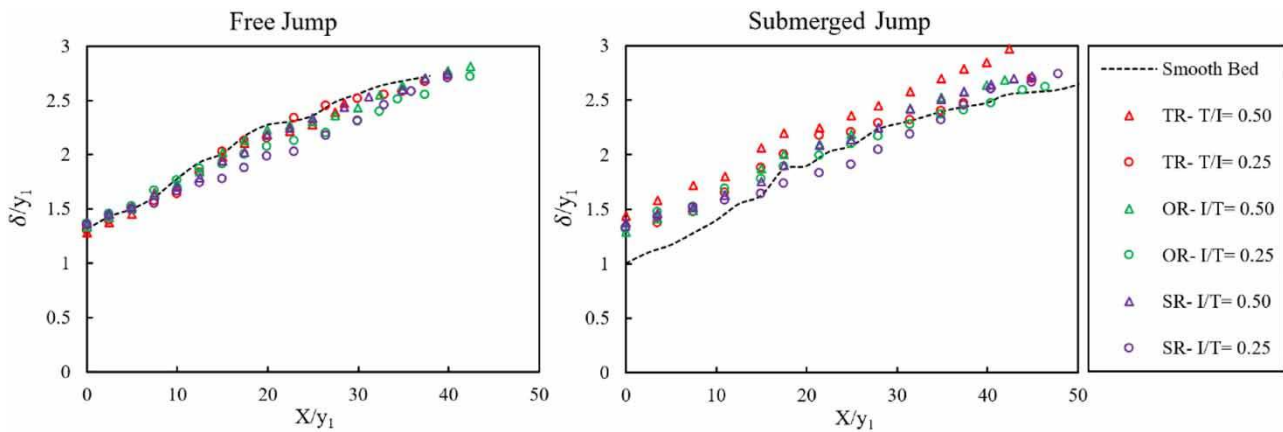


**Figure 8** | Variations of ($\delta/y_1$) versus ($X/y_1$) for different roughness shape.

hydraulic jump, the position of maximum velocity (i.e., the thickness of the inner layer of the horizontal velocity distribution) increases. Also, the thickness of the boundary layer decreases with increasing distance between the roughnesses on the macroroughnesses (TR, OR and SR). The lowest value of $\delta/y_1$ is related to $T/I = 0.25$, while its highest value is related to $T/I = 0.50$ in different modes. The triangular macroroughness shows the maximum values of the boundary layer thickness. Based on the above findings, for macroroughnesses (TR, OR and SR) and for all $T/I$ ratios, $U_m/u_1$ and $\delta/y_1$ of free and submerged jumps can be estimated through the following equations, respectively:

$$\frac{U_m}{u_1} = 2.050\left(\frac{X}{y_1}\right)^{-0.633}, \quad R^2 = 0.906 \tag{15}$$

$$\frac{U_m}{u_1} = 1.573\left(\frac{X}{y_1}\right)^{-0.494}, \quad R^2 = 0.816 \tag{16}$$

$$\frac{\delta}{y_1} = 0.035\left(\frac{X}{y_1}\right) + 1.375, \quad R^2 = 0.956 \tag{17}$$

$$\frac{\delta}{y_1} = 0.032\left(\frac{X}{y_1}\right) + 1.339, \quad R^2 = 0.911 \tag{18}$$

The dimensionless values ($U_m/u_1$) and ($\delta/y_1$) in free and submerged jumps over the smooth and rough bed are shown in Figure 9. The results of the present study are compared with the experimental data by Abbaspour *et al.* (2009), Shekari *et al.* (2014) and Pourabdollah *et al.* (2019). For the smooth bed, the maximum flow velocity at the beginning of the jump for the free jump is more than the submerged jump, but at the end of the jump, these values are higher
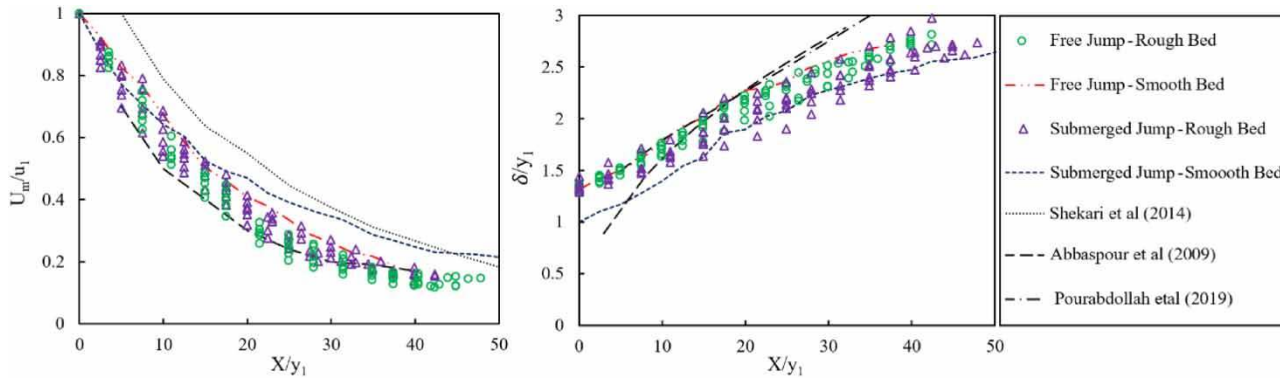
**Figure 9** | Variations of the dimensionless parameters ($U_m/u_1$) and ($\delta/y_1$) in free and submerged jumps.

for the submerged jump. In the rough bed, the dimensionless ratio ($U_m/u_1$) at a specified $X$ in the submerged jump is higher than in the free jump. This finding agrees with previous research by Pourabdollah *et al.* (2019). In addition, for both smooth and rough bed in the submerged jump due to increasing depth and eddy flow, the maximum velocity distance from the bed is reduced and the boundary layer thickness is less than free jump. The results of the present study are in good agreement with the data by Abbaspour *et al.* (2009) and Pourabdollah *et al.* (2019) and there is a discrepancy in ($U_m/u_1$) with the results by Shekari *et al.* (2014) because this researcher studied only the smooth bed.

## Bed shear stress

The roughness bed increases the bed shear stress and reduces the sequent water depth and the length of the hydraulic jump (Ead & Rajaratnam 2002; Samadi-Boroujeni *et al.* 2013; Pourabdollah *et al.* 2019). As a result, it leads to a reduction in the length of the stilling basin. The shear stress coefficient ($\varepsilon$) is calculated as follows (Rajaratnam 1965):

$$\varepsilon = \frac{F_\tau}{0.5\gamma y_1^2} \tag{19}$$

where $F_\tau$ is shear force per unit width and can be obtained using the following equations for the free and submerged jumps, respectively:

$$F_1 - F_2 - F_\tau = \rho q(\beta_2 V_2 - \beta_1 V_1) \tag{20}$$

$$F_3 - F_4 - F_\tau = \rho q(\beta_4 V_4 - \beta_1 V_1) \tag{21}$$

where $F_1 = 0.5\gamma y_1^2$, $F_2 = 0.5\gamma y_2^2$, $F_3 = 0.5\gamma y_3^2$ and $F_4 = 0.5\gamma y_4^2$ represent, respectively, the hydrostatic pressure forces imposed on the control volume at sections 1, 2, 3 and 4 that are related to $y_1$, $y_2$, $y_3$ and $y_4$. The symbols $\beta_1$, $\beta_2$ and $\beta_4$ are the momentum correction factors at sections 1, 2 and 4, which were assumed to be equal to 1 (Pourabdollah *et al.* 2019). $\gamma$ is the specific weight, $q$ is the flow rate in width unit, and $V_1$, $V_2$ and $V_4$ are the average velocities at the initial jump (section 1), at sections 2 and 4, respectively. The value of the bed shear force coefficient was determined by using Equation (19). Figure 10 shows the variations of shear stress coefficient ($\varepsilon$) of the free and submerged jumps as a function of the inlet Froude number ($Fr_1$). The numerical results of the shear stress coefficient were compared with Ead & Rajaratnam (2002) (Equations (22) and (23) for the hydraulic jump on the smooth bed and macroroughnesses, respectively) and Izadjoo & Shafai Bajestan (2007) (experimental data and Equation (24)) for free jump, and Pourabdollah *et al.* (2019) (Equation (25)) for the submerged jump, respectively:

$$\varepsilon = 0.16Fr_1^2 - 0.8Fr_1 + 1 \tag{22}$$

$$\varepsilon = (Fr_1 - 1)^2 \tag{23}$$

$$\varepsilon = 0.058Fr_1^{3.035} \tag{24}$$

$$\varepsilon = 0.7485Fr_1^{1.5} \tag{25}$$

It can be seen from Figure 10 that the shear stress coefficient ($\varepsilon$) generally increases with the increasing inlet Froude number ($Fr_1$). The value of $\varepsilon$ of the free and submerged
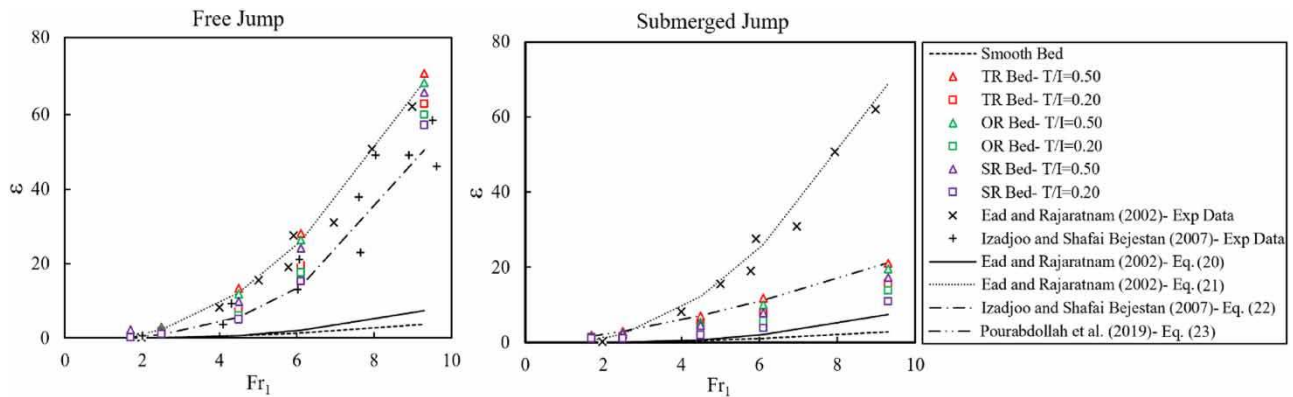
**Figure 10** | Variation of shear force coefficient ($\varepsilon$) versus different inlet Froude number ($Fr_1$).

jumps on the macroroughnesses (TR, OR and SR) is more than the smooth bed. The highest shear stress occurs in a triangular macroroughness (TR) with $T/I = 0.50$ for both the free and the submerged jumps compared to other ratios ($T/I = 0.33$, $0.25$ and $0.20$) and roughnesses (OR and SR). Also, the value of the shear stress coefficient in the submerged jump was more for the smooth bed and less for the free jump.

In general, based on the results drawn from this study, the following equations for the shear stress coefficient in macroroughnesses (TR, OR and SR) for all ratios and roughnesses with a good correlation coefficient were obtained for the free and submerged jumps, respectively:

$$\varepsilon = 0.084 Fr_1^{2.982}, \quad R^2 = 0.989 \tag{26}$$

$$\varepsilon = 0.454 Fr_1^{1.532}, \quad R^2 = 0.929 \tag{27}$$

## Sequent depth ratio and submerged depth ratio

Figure 11 shows the values of ($y_2/y_1$) versus ($Fr_1$) and a comparison between numerical data and experimental results obtained from Tokyay (2005) in the free jump is performed. As can be seen, the sequent depth ratio ($y_2/y_1$), which somehow represents the height of the jump, is directly related to the changes in the inlet Froude number ($Fr_1$) and the distance of roughness element, and by increasing these parameters, the value ($y_2/y_1$) is increased. In other words, the reduction of the boundary layer thickness will further increase the effect of
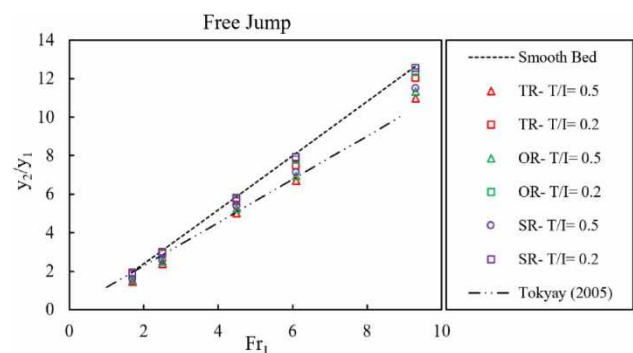


**Figure 11** | Sequent depth ratio ($y_2/y_1$) versus ($Fr_1$).

roughness and intensify the reduction of the sequent depth ratio. Also, this slight decrease can be attributed to the increase in the flow separation and recirculation vortex moving between the roughnesses, which increases with increasing the inlet Froude number. The greatest reduction of sequent depth ratio ($y_2/y_1$) occurs in triangular macroroughnesses for $T/I = 0.5$ compared to other shapes and ratios.

One of the important characteristics of the submerged jump is the submergence depth on the gate ($y_3$) which is needed to calculate the initial energy of the submerged jump. Therefore, the submerged depth ratio ($y_3/y_1$), as well as the tailwater depth ratio of the submerged jump ($y_4/y_1$) versus the inlet Froude number ($Fr_1$), are shown in Figure 12. According to Figure 12, by increasing the inlet Froude number, both parameters ($y_3/y_1$) and ($y_4/y_1$) are increased for the different distances between the roughnesses. The results of the present study have good agreement with previous research by Ahmed *et al.* (2014). The results showed
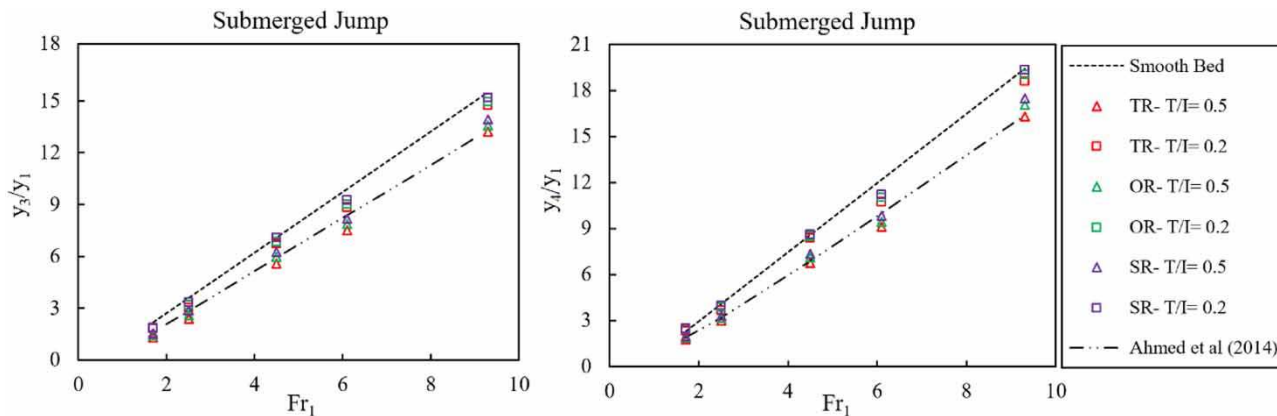
**Figure 12** | Submerged depth ratio ($y_3/y_1$) and tailwater depth ratio ($y_4/y_1$) versus $Fr_1$.

that the reduction in the values of $y_3/y_1$ and $y_4/y_1$ depends mainly on the space of the roughnesses, in which the vortex flow forms. For this reason, for $T/I = 0.5$, the values of $y_3/y_1$ and $y_4/y_1$ decrease by about 20.87% and 23.34% as a mean, respectively. The values of the ratio of these depths in the macroroughnesses are always less than in the smooth bed. The following equations describe the relationship of the sequent depth, submerged depth and tailwater depth ratios versus Froude number in macroroughnesses with all ratios for free and submerged jumps, respectively:

$$\frac{y_2}{y_1} = 1.249Fr, \quad R^2 = 0.998 \tag{28}$$

$$\frac{y_3}{y_1} = 1.431Fr + 7.670S - 2.891, \quad R^2 = 0.997 \tag{29}$$

$$\frac{y_4}{y_1} = 1.769Fr_1 + 9.602S - 3.688, \quad R^2 = 0.992 \tag{30}$$

### The relative length of jumps

Figure 13 shows the dimensionless relative length of the jump ($L_j/y_{2*}$) versus inlet Froude numbers ($Fr_1$) for ratios $T/I = 0.2$ and 0.5 with different roughness shapes and smooth bed. It shows that in all modes, the length of the jump for the macroroughnesses is less than the smooth bed and for the submerged jump larger than the free jump. This finding agrees with the results obtained by Tokyay *et al.* (2011). Also, the value of $L_j/y_{2*}$ for $T/I = 0.2$ is greater

than $T/I = 0.5$. Apart from some cases related to specific Froude numbers, the results show that the relative length of jump generally increases with increasing inlet Froude numbers, particularly for the case of the submerged jump. By comparing the types of roughness shapes, the triangular macroroughnesses have a significant effect on the length of the jump and show the shortest length with respect to other shapes. In Figure 14, the ratio length of the jump ($L_j/y_1$) for triangular macroroughnesses was plotted at $0.2 < T/I < 0.5$ versus different inlet Froude numbers ($Fr_1$). It can be seen that with increasing distance between roughnesses, the length of the jump for both jumps increases and acts as a smooth bed. For $T/I = 0.5$, the ratio length of the jump decreases by about 25.52% as a mean. Therefore, it is recommended that to reduce the length of the jump to achieve the shortest length of the stilling basins, the triangular macroroughnesses with near-roughness elements ($T/I = 0.5$) can be used in the stilling basins. The following equations show the relationships of the ratio length of jumps versus Froude numbers that were obtained for the free and submerged jumps, respectively, and for macroroughnesses (TR, OR and SR) and all ratios:

$$\frac{L_{jf}}{y_{2*}} = 0.043Fr_1 + 5.432, \quad R^2 = 0.708 \tag{31}$$

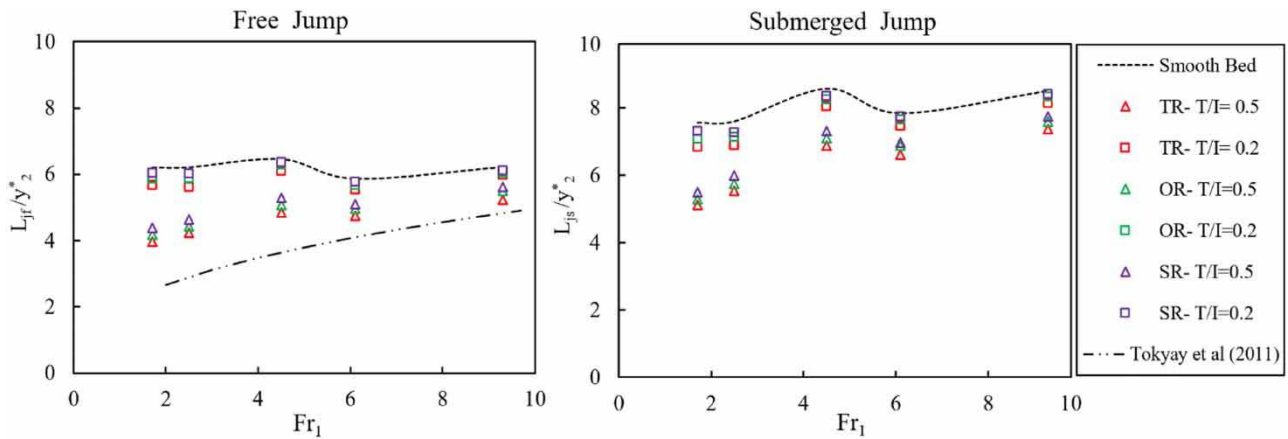$$\frac{L_{js}}{y_{2*}} = -0.084Fr_1 + 8.909S + 4.368, \quad R^2 = 0.887 \tag{32}$$

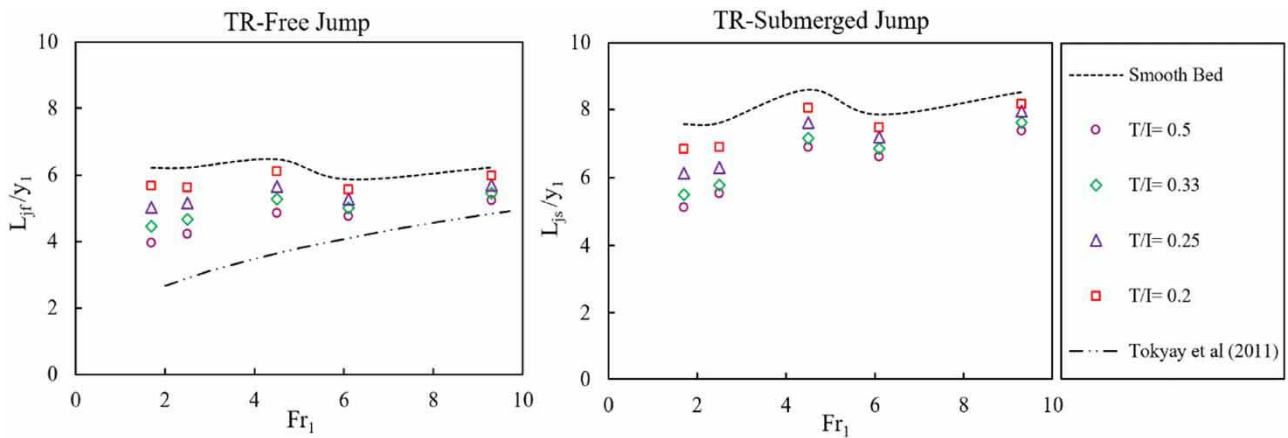**Figure 13** | Variation of $L_j/y_2*$ versus $Fr_1$ for different roughness shape.



**Figure 14** | Variation of $L_j/y_1$ versus $Fr_1$ for triangular macroroughness.

## Energy loss

The relative energy loss of free and submerged jumps can be calculated as follows (Pourabdollah et al. 2019):

$$\frac{\Delta E}{E_1} = \frac{E_1 - E_2}{E_1} = \frac{(y_1 + V_1^2/2g) - (y_2 + V_2^2/2g)}{y_1 + V_1^2/2g} \tag{33}$$

$$\frac{\Delta E}{E_1} = \frac{E_3 - E_4}{E_3} = \frac{(y_3 + V_1^2/2g) - (y_4 + V_4^2/2g)}{y_3 + V_1^2/2g} \tag{34}$$

where $E_1$, $E_2$, $E_3$ and $E_4$ are specific energies upstream and downstream of the free and submerged jumps, respectively (see Figure 1). Figure 15 shows the relative energy loss of free and submerged jumps versus inlet

Froude number ($Fr_1$). It can be seen that the dimensionless ratio $\Delta E/E_1$ increases with the increasing the inlet Froude number ($Fr_1$). Figure 15 indicates that the energy loss of the free jump was greater than that of the submerged jump. Also, for the same inlet Froude number, the energy loss on macroroughnesses (TR, OR, SR) is greater than that of the smooth bed. The results of the energy loss compared with previous experimental data. In particular, these findings are in acceptable agreement with the results of Pourabdollah et al. (2019). By increasing the distance between the roughnesses and inlet Froude number, the energy loss decreases for all the macroroughnesses (TR, OR, SR) in both jumps. The highest $\Delta E/E_1$ occurs in a triangular macroroughness (TR) with $T/I = 0.50$ in the free and submerged jumps
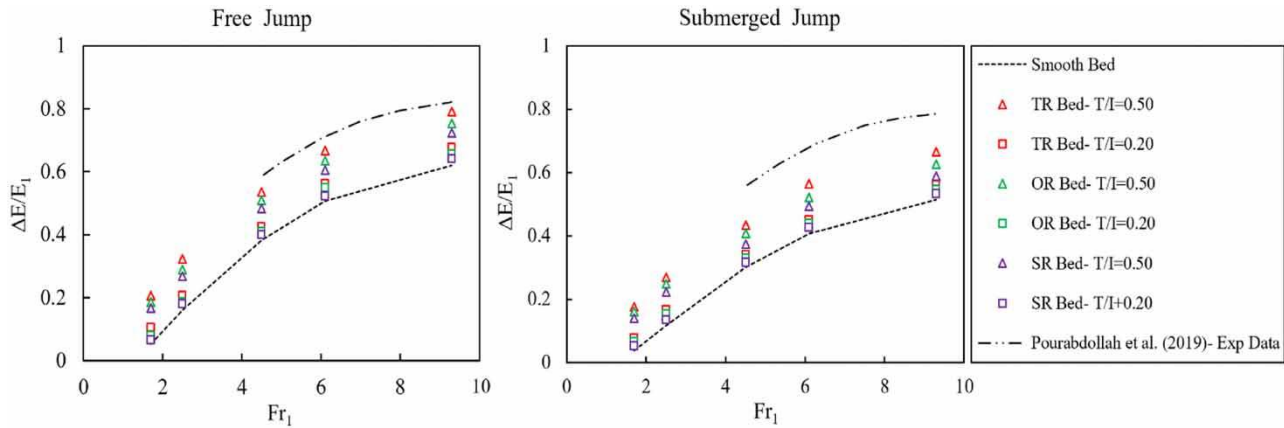
**Figure 15** │ The energy loss ($\Delta E/E_1$) of free and submerged jumps versus inlet Froude number ($Fr_1$).

compared to other ratios and modes. In general, for all macroroughnesses based on the numerical data of the present study, the relationships provided for the free and submerged jumps are expressed as:

$$\frac{\Delta E}{E_1} = -0.0104 Fr_1^2 + 0.191 Fr_1 - 0.205, \ R^2 = 0.961 \qquad (35)$$

$$\frac{\Delta E}{E_1} = -0.0073 Fr_1^2 + 0.144 Fr_1 - 0.148, \ R^2 = 0.955 \qquad (36)$$

## CONCLUSIONS

In this study, the characteristics of free and submerged hydraulic jumps including horizontal velocity distribution, bed shear stress, sequent and submerged depth ratio, hydraulic jump length and energy loss over the different shapes of macroroughnesses were numerically investigated using FLOW-3D model. To simulate the flow turbulence at hydraulic jumps, the RNG $k$–$\varepsilon$ turbulence model was chosen. The results of this study are briefly summarized as follows:

- The maximum MSE and MARE errors between numerical results and experimental data of Ahmed *et al.* (2014) on a smooth bed are 4.21% and 0.188, respectively, that confirms the ability of the numerical model to predict the specifications of free and submerged jumps.
- The relative maximum horizontal velocity in the macroroughnesses is less than in the smooth bed and the

effect of roughness plays a role in the reduction of this parameter and is greater in the submerged jump.
- The thickness of the boundary layer decreases with increasing distance between the roughnesses and increases with increasing the distance from the beginning of the hydraulic jump.
- The reduction of the boundary layer thickness will further increase the effect of roughness and intensify the reduction of the sequent depth ratio. The reduction of this ratio ($y_2/y_1$) for the triangular macroroughnesses is greater than the square and semi-oval one.
- The ratio length of the jump for $T/I = 0.5$ of rough bed decreases by about 25.52% than a smooth bed and increases with increasing distance between roughnesses.
- By comparing the types of roughness shapes, the triangular macroroughnesses have a significant effect on the length of the jump and lead to the shortest length with respect to the other shapes.
- The reduction in the submerged depth ratio ($y_3/y_1$) and the tailwater depth ratio ($y_4/y_1$) depends mainly on the space between the macroroughness, in which the vortex flow forms. For $T/I = 0.5$, the values of ($y_3/y_1$) and ($y_4/y_1$) decrease by about 20.87 and 23.34% as a mean, respectively. The values of the ratio of these depths in the macroroughness are always less than in the smooth bed.
- The value of shear stress coefficient ($\varepsilon$), energy loss, the submerged depth ratio ($y_3/y_1$), the tailwater depth ratio and, generally, the relative length of jump in free and submerged jumps ($y_2/y_1$) or ($y_4/y_1$) increases with the increasing inlet Froude number ($Fr_1$). The highest shear

stress and energy loss in the free and submerged jumps occur in a triangular macroroughness (TR) with $T/I =$ 0.50 compared to other ratios and modes.

Overall, CFD models may provide very good predictions of characteristics of free and submerged jumps through different hydraulic conditions and various geometrical arrangements. Velocity field, bed shear stress and specifications of the hydraulic jump can be simulated with a numerical solution. However, the analysis of the roughness height on flow field alteration and TKE as a future work remains still an issue to be faced.

## DATA AVAILABILITY STATEMENT

All relevant data are included in the paper or its Supplementary Information.

## REFERENCES

Abbaspour, A., Dalir, A. H., Farsadizadeh, D. & Sadraddini, A. A. 2009 Effect of sinusoidal corrugated bed on hydraulic jump characteristics. *Journal of Hydro-Environment Research* **3** (2), 109–117.

Abbaspour, A., Taghavianpour, T. & Arvanaghi, H. 2019 Experimental study of the hydraulic jump on reverse bed with porous screens. *Applied Water Science* **9** (7), 155.

Ahmed, H. M. A., El Gendy, M., Mirdan, A. M. H., Ali, A. A. M. & Haleem, F. S. F. A. 2014 Effect of corrugated beds on characteristics of submerged hydraulic jump. *Ain Shams Engineering Journal* **5** (4), 1033–1042.

Akib, S., Ahmed, A. A., Imran, H. M., Mahidin, M. F., Ahmed, H. S. & Rahman, S. 2015 Properties of hydraulic jump over apparent corrugated beds. *Dam Engineering* **25** (2), 65–77.

AlTalib, A. N., Mohammed, A. Y. & Hayawi, H. A. 2019 Hydraulic jump and energy dissipation downstream stepped weir. *Flow Measurement and Instrumentation* **69**, 101616.

Bayon, A., Valero, D., García-Bartual, R. & López-Jiménez, P. A. 2016 Performance assessment of OpenFOAM and FLOW-3D in the numerical modeling of a low Reynolds number hydraulic jump. *Environmental Modelling and Software* **80**, 322–335.

Bayon-Barrachina, A. & Lopez-Jimenez, P. A. 2015 Numerical analysis of hydraulic jumps using OpenFOAM. *Journal of Hydroinformatics* **17** (4), 662–678.

Bradley, J. N. & Peterka, A. J. 1957 The hydraulic design of stilling basins: hydraulic jumps on a horizontal apron (basin i). *Journal of the Hydraulics Division* **83** (5), 1–24.

Carvalho, R. & Lemos Ramo, C. 2008 Numerical computation of the flow in hydraulic jump stilling basins. *Journal of Hydraulic Research* **46** (6), 739–752.

Celik, I. B., Ghia, U. & Roache, P. J. 2008 Procedure for estimation and reporting of uncertainty due to discretization in CFD applications. *Journal of Fluids Engineering* **130** (7), 0780011–0780013.

Chanson, H. 2009 Development of the Bélanger equation and backwater equation by Jean-Baptiste Bélanger (1828). *Journal of Hydraulic Engineering* **135** (3), 159–163.

Choufu, L., Abbasi, S., Pourshahbaz, H., Taghvaei, P. & Tfwala, S. 2019 Investigation of flow, erosion, and sedimentation pattern around varied groynes under different hydraulic and geometric conditions: a numerical study. *Water* **11** (2), 235.

Chow, V. T. 1959 *Open Channel Hydraulics*. McGraw-Hill, New York.

Daneshfaraz, R., Ghahramanzadeh, A., Ghaderi, A., Joudi, A. R. & Abraham, J. 2016 Investigation of the effect of edge shape on characteristics of flow under vertical gates. *Journal of American Water Works Association* **108** (8), 425–432.

Daneshfaraz, R., Minaei, O., Abraham, J., Dadashi, S. & Ghaderi, A. 2019 3-D numerical simulation of water flow over a broad-crested weir with openings. *ISH Journal of Hydraulic Engineering* 1–9. doi: 10.1080/09715010.2019.1581098

Dey, S. & Sarkar, A. 2008 Characteristics of turbulent flow in submerged jumps on rough beds. *Journal of Engineering Mechanics* **134** (1), 49–59.

Ead, S. A. & Rajaratnam, N. 2002 Hydraulic jumps on corrugated beds. *Journal of Hydraulic Engineering* **128** (7), 656–663.

Federico, I., Marrone, S., Colagrossi, A., Aristodemo, F. & Antuono, M. 2012 Simulating 2D open-channel flows through an SPH model. *European Journal of Mechanics-B/Fluids* **34**, 35–46.

Felder, S. & Chanson, H. 2018 Air–water flow patterns of hydraulic jumps on uniform beds macroroughness. *Journal of Hydraulic Engineering* **144** (3), 04017068.

Flow Science Inc 2016 *FLOW-3D V 11.2 User's Manual*. Santa Fe, NM, USA.

Garcia Perez, M. & Vakkilainen, E. 2019 A comparison of turbulence models and two and three dimensional meshes for unsteady CFD ash deposition tools. *Fuel* **237**, 806–811.

Ghaderi, A. & Abbasi, S. 2019 CFD simulation of local scouring around airfoil-shaped bridge piers with and without collar. *Sādhanā* **44** (10), 216.

Ghaderi, A., Dasineh, M., Abbasi, S. & Abraham, J. 2020a Investigation of trapezoidal sharp-crested side weir discharge coefficients under subcritical flow regimes using CFD. *Applied Water Science* **10** (1), 1–12.

Ghaderi, A., Abbasi, S., Abraham, J. & Azamathulla, H. M. 2020b Efficiency of trapezoidal labyrinth shaped stepped spillways. *Flow Measurement and Instrumentation* **72**, 101711.

Ghaderi, A., Dasineh, M., Daneshfaraz, R. & Abraham, J. 2020c Reply to the discussion on paper: 3-D numerical simulation of water flow over a broad-crested weir with openings by Daneshfaraz *et al.*, 2019, in ISH Journal of Hydraulic

Engineering. *ISH Journal of Hydraulic Engineering.* (in press). doi:10.1080/09715010.2019.1581098.

Ghaderi, A., Daneshfaraz, R., Dasineh, M. & Di Francesco, S. 2020d Energy dissipation and hydraulics of flow over trapezoidal–triangular labyrinth weirs. *Water* **12** (7), 1992.

Ghaderi, A., Daneshfaraz, R., Abbasi, S. & Abraham, J. 2020e Numerical analysis of the hydraulic characteristics of modified labyrinth weirs. *International Journal of Energy and Water Resources*, 1–12.

Habibzadeh, A., Rajaratnam, N. & Loewen, M. 2019 Characteristics of the flow field downstream of free and submerged hydraulic jumps. *Proceedings of the Institution of Civil Engineers-Water Management.* **172** (4), 180–194.

Hager, W. H. 1993 Classical hydraulic jump: free surface profile. *Canadian Journal of Civil Engineering* **20** (3), 536–539.

Hager, W. H., Bremen, R. & Kawagoshi, N. 1990 Classical hydraulic jump: length of roller. *Journal of Hydraulic Research* **28** (5), 591–608.

Hassanpour, N., Hosseinzadeh Dalir, A., Farsadizadeh, D. & Gualtieri, C. 2017 An experimental study of hydraulic jump in a gradually expanding rectangular stilling basin with roughened bed. *Water* **9** (12), 945.

Helal, E., Abdelhaleem, F. S. & Elshenawy, W. A. 2020 Numerical assessment of the performance of bed water jets in submerged hydraulic jumps. *Journal of Irrigation and Drainage Engineering* **146** (7), 04020014.

Hirt, C. W. & Nichols, B. D. 1981 Volume of fluid (VOF) method for the dynamics of free boundaries. *Journal of Computational Physics* **39**, 201–225.

Hirt, C. W. & Sicilian, J. M. 1985 *A Porosity Technique for the Definition of Obstacles in Rectangular Cell Meshes.* Flow Science, New Mexico.

Izadjoo, F. & Shafai-Bejestan, M. 2007 Corrugated bed hydraulic jump stilling basin. *Journal of Applied Sciences* **7** (8), 1164–1169.

Long, D., Steffler, P. M. & Rajaratnam, N. 1990 LDA study of flow structure in submerged hydraulic jumps. *Journal of Hydraulic Research* **28** (4), 437–460.

Lopardo, R. A. 2013 Extreme velocity fluctuations below free hydraulic jumps. *Journal of Engineering* **2013**, 1–5. doi: 10.1155/2013/678064.

Matin, M. A., Hasan, M. & Islam, M. R. 2008 Experiment on hydraulic jump in sudden expansion in a sloping rectangular channel. *Journal of Civil Engineering (IEB)* **36** (2), 65–77.

Mouaze, D., Murzyn, F. & Chaplin, J. R. 2005 Free surface length scale estimation in hydraulic jumps. *Journal of Fluids Engineering* **127**, 1191–1193.

Pourabdollah, N., Heidarpour, M. & Abedi Koupai, J. 2019 Characteristics of free and submerged hydraulic jumps in different stilling basins. In *Proceedings of the Institution of Civil Engineers-Water Management.* Thomas Telford Ltd, pp. 1–11.

Rajaratnam, N. 1965 The hydraulic jump as a well jet. *Journal of the Hydraulics Division* **91** (5), 107–132.

Rajaratnam, N. 1968 Hydraulic jump on rough bed. *Transactions of the Engineering Institute of Canada* **11** (2), 1–8.

Rao, N. S. & Rajaratnam, N. 1963 The submerged hydraulic jump. *Journal of the Hydraulics Division* **89** (1), 139–162.

Roushangar, K. & Ghasempour, R. 2019 Evaluation of the impact of channel geometry and rough elements arrangement in hydraulic jump energy dissipation via SVM. *Journal of Hydroinformatics* **21** (1), 92–103.

Salim, M. S. & Cheah, S. C. 2009 Wall y+ strategy for dealing with wallbounded turbulent flows. In *Proceedings of the International Multiconference of Engineers and Computer Scientists.* Vol II, IMECS, Hong Kong.

Samadi-Boroujeni, H., Ghazali, M., Gorbani, B. & Nafchi, R. F. 2013 Effect of triangular corrugated beds on the hydraulic jump characteristics. *Canadian Journal of Civil Engineering* **40** (9), 841–847.

Samma, H., Khosrojerdi, A., Rostam-Abadi, M., Mehraein, M. & Cataño-Lopera, Y. 2020 Numerical simulation of scour and flow field over movable bed induced by a submerged wall jet. *Journal of Hydroinformatics* **22** (2), 385–401.

Sangsefidi, Y., MacVicar, B., Ghodsian, M., Mehraein, M., Torabi, M. & Savage, B. M. 2019 Evaluation of flow characteristics in labyrinth weirs using response surface methodology. *Flow Measurement and Instrumentation* **69**, 101617.

Shekari, Y., Javan, M. & Eghbalzadeh, A. 2014 Three-dimensional numerical study of submerged hydraulic jumps. *Arabian Journal for Science and Engineering* **39** (10), 6969–6981.

Tokyay, N. D. 2005 Effect of channel bed corrugations on hydraulic jumps. *Impacts of Global Climate Change, World Water and Environmental Resources Congress*, 1–9. doi: 10.1061/40792(173)408.

Tokyay, N. D., Evcimen, T. U. & Şimşek, Ç. 2011 Forced hydraulic jump on non-protruding rough beds. *Canadian Journal of Civil Engineering* **38** (10), 1136–1144.

Torkamanzad, N., Hosseinzadeh Dalir, A., Salmasi, F. & Abbaspour, A. 2019 Hydraulic jump below abrupt asymmetric expanding stilling basin on rough bed. *Water* **11** (9), 1756.

Vischer, D. L. & Hager, W. H. 1995 Energy dissipators. In: *Hydraulic Structures Design Manual*, 1st edn, (A. A. Balkema, ed.). IAHR, Rotterdam, Netherlands. ISBN-10:9054101989.

Witt, A., Gulliver, J. S. & Shen, L. 2018 Numerical investigation of vorticity and bubble clustering in an air entraining hydraulic jump. *Computers & Fluids* **172**, 162–180.

Woodward, S. M. 1917 *Theory of the Hydraulic Jump and Backwater Curves.* State of Ohio, Miami Conservancy District.

Wu, S. & Rajaratnam, N. 1995 Free jumps, submerged jumps and wall jets. *Journal of Hydraulic Research* **33** (2), 197–212.

Yakhot, V. & Orszag, S. A. 1986 Renormalization group analysis of turbulence. I. Basic theory. *Journal of Scientific Computing* **1** (1), 3–51.

Zahabi, H., Torabi, M., Alamatian, E., Bahiraei, M. & Goodarzi, M. 2018 Effects of geometry and hydraulic characteristics of shallow reservoirs on sediment entrapment. *Water* **10** (12), 1725.